Spectrochimica Acta Part B: Atomic Spectroscopy 216 (2024) 106949

Contents lists available at ScienceDirect

Spectrochimica Acta Part B: Atomic Spectroscopy

journal homepage: www.elsevier.com/locate/sab

Spatially resolved spectroscopical characterization of one- and two-component structured femtosecond laser induced plasmas

Cristina Méndez-López, Cristina González-Gago, Jorge Pisonero, Nerea Bordel *

University of Oviedo, Department of Physics, Federico García Lorca 18, 33007 Oviedo, Asturias, Spain

ARTICLE INFO

Keywords:
LIBS
Femtosecond ablation
Spatio-temporal resolution
Plasma diagnostics

ABSTRACT

Femtosecond-laser ablation is becoming increasingly popular due to its advantageous characteristics such as reduced fractionation and improved lateral resolution. However, since the emission from the resulting laser-induced plasmas is reduced and relatively short-lived, optical spectroscopy analyses with fs lasers (LIBS) are often carried out with enhancement strategies, such as double-pulse LIBS. For orthogonal double pulse set ups, characterizing the spatio-temporal excitation of the fs-LIP can be useful to fully optimize the scheme. This work aims to characterize the structure of a fs-laser induced plasma in atmospheric pressure, illustrating the general behavior of the plasma plume for different target materials (metals and dielectrics), and further obtain insight about the emission and excitation characteristics of the plume for pure copper and PVC samples. The results show a clear two-component structure of the metallic plumes, composed by a fast-displacing upper component that presents higher excitation and higher ionization degree and a slow, almost static component that remains near the sample surface throughout the complete evolution. On the contrary, PVC presented only one fast-displacing component which was seen not to be homogeneous in terms of excitation. As a general feature, in the present study conditions, all the plasma plumes induced in different samples presented an intensity-dominating fast component, with discrepancies in the presence and relative intensity of the slow component.

1. Introduction

Laser-Induced Breakdown Spectroscopy (LIBS) is a well-stablished analytical technique that consists in the use of a pulsed laser that, by focusing it onto a sample, produces a transient plasma, whose emission is analysed. LIBS stands out by its intrinsic versatility [1]; it can deal with samples of vastly different nature, and it is instrumentally very flexible in terms of complexity, portability, and hyphenation with other techniques (e.g. LIBS-Raman [2–4] or LIBS-LA-ICP-MS [5–7]). Despite the simplicity of its operating principle, the physics behind the laser-matter interaction process as well as the laser-induced plasma dynamics are complicated. Many experimental parameters are relevant in this regard, one of them being the laser pulse duration [8,9]. Nanosecond-lasers are undoubtedly the most frequently utilized sources of excitation in LIBS, but femtosecond lasers have attracted increasing interest during recent years [10].

Nanosecond-pulsed ablation is an intrinsically thermal process characterized by sequential mechanisms such as melting, fusion, sublimation, and vaporization, with heat diffusion increasing the area of damage [11]. Moreover, the vaporized matter further interacts with the laser beam increasing ionization and excitation but also eventually resulting in a shielding process due to inverse Bremsstrahlung (more pronounced for IR wavelengths), which prevents energy being deposited on the sample, reducing ablation rate. The effect of shielding, however, is not entirely undesirable as it results in a bright, excited, and long-lived (tens of microseconds) plasma [12]. The ultrashort pulse regime, on the other hand, is characterized by energy deposition taking place faster than the lattice relaxation time. This has several consequences both in the solid ablation process and in the resulting plasma characteristics. The most important aspect is that the laser energy is absorbed in a reduced area of interaction, resulting in a high ablation rate and well-defined craters (i.e. lateral resolution improvement). The lack of laser-plasma interaction, however, means that fs-LIPs often must be somehow re-excited to improve the emission signal (e.g. in double-pulse LIBS arrangements [13]). As for the mechanisms responsible for the ablation in this regime, thorough discussions can be found in [10,14,15] and will be described only briefly here. Said mechanisms vary depending on pulse energy and sample characteristics (i.e. conducting, dielectrics).

* Corresponding author.
E-mail address: bordel@uniovi.es (N. Bordel).

https://doi.org/10.1016/j.sab.2024.106949
Received 31 January 2024; Received in revised form 17 May 2024; Accepted 20 May 2024
Available online 21 May 2024

For metals, free electrons are notably excited through inverse Bremsstrahlung and multiphoton (MP) absorption, which will be favored for longer and shorter wavelengths, respectively. The energized electrons can undergo collisions with other electrons, or even leave the solid target and produce an electrostatic field in the vicinity of the surface that, in turn, pulls ions out of the solid ("electrostatic ablation"). Coulomb explosion, caused by the repulsive forces of the positively charged ions in the surface of the sample, is also regarded as one of the main mechanisms in the ablation of dielectrics, whereas high irradiance values are needed for its occurrence in metals. Another important mechanism is thermal vaporization, which results from the temperature increase due to electron-phonon collisions at timescales (ps) longer than the laser pulse width.

The resulting plasma plume is conditioned by the several mechanisms that might have taken part in the ablation [16–19]. Time-of-flight studies carried out in vacuum on a Ti sample by Albert et al. showed the presence of three differentiated components consisting on fast ions, slower neutrals and very slow nanocluster population emitting characteristic blackbody radiation at long delay times (>μs) [16]. Grojo et al. ablated Ti, Zr and Hf samples in a low-pressure helium atmosphere, observing a fast-displacing component containing ions and atoms and a slow component with emitting nanoparticles [17]. Noël et al. studied fs-LIPs on Au and Cu samples, reporting a clear dominance in emission intensity of the lower region of the plasma plume, which was induced in vacuum. Spectroscopical analysis of the copper plasma highlighted spatially separated predominance of nanoparticles, neutrals and ions [18]. For dielectric materials, Axente et al. observed the formation of a single component when ablating fused silica in vacuum, lacking presence of nanoparticles [19]. Recent works by Kautz et al. dealt with the ablation of a zircaloy sample in a He low-pressure environment, also noting the absence of continuum emission from nanoparticles and additionally reporting higher excitation temperatures region of the plasma plume closer to the sample surface [20,21].

Aside from sample nature, the plume dynamics are also affected by experimental conditions such as ambient pressure [22], lens-to-sample distance [21,23] and fluence [24]. The expansion of the plume is, of course, very dependent on the former, observing a greater extent of expansion as well as a spherical symmetry in vacuum as compared to confined, cylindrical plumes at atmospheric pressure [22]. However, displacement of the sample from the focal plane (modifying fluence and spot size) in a vacuum result in narrower angular distribution [23]. Notable variation of the relative intensity and lifetime of the fast component in the plasma plume was also reported [21]. Increasing fluence at a fixed spot size allowed for higher emission intensities of both atoms and ions, also providing a higher ionization degree in a copper plume. On the other hand, electron density was seen to rapidly maximize at an intermediate fluence (10 J/cm^2), slightly decreasing with greater fluences. Similarly, excitation temperature could be increased with pulse energy until it plateaued at a similar fluence [24].

A partial or complete plume splitting in atmospheric environment can be attributed to an ambipolar electric field as a consequence of the spatial separation of charged species, as modelled and experimentally demonstrated utilizing a brass sample by Zhang et al. in a recent work [25]. Particularly, they reported an increased separation between components for shorter pulse durations and higher fluence, as well as earlier split of the plume with smaller spot sizes. Additionally, fs-laser filamentation can also occur and result in weak ionization of air along the laser propagation path due to non-linear process of filamentation if laser power is sufficient to result in self-focusing. This effect was studied by Hou et al. on a Zr sample, noting that the lower density region created by the filament promotes a narrow vertical plume expansion that can result in a clear split of the plume, depending on the lens-to-sample distance, creating a high temperature environment with low continuum emission [26]. An analogous work by Xu et al. performed on a copper sample detailed the dependance of both temperature and electron density with lens-to-sample distance, also observing the simultaneous increase/decrease in excitation temperature/electron density, despite lacking spatial resolution in the spectral analysis [27]. Thus, focusing conditions and laser power have to be taken into account in order to attribute plume splitting to either mechanism.

In the present work, an infrared (1028 nm) fs-LIBS system operated at ambient pressure conditions is utilized to perform, as a first step, a general comparison of the plasma plume behavior at few shots per spot for several targets of different nature (metallic and dielectric), exploring the extent of potential differences in their spatio-temporal evolution with regard of plume splitting as well as relative intensity of plume components. Afterwards, a > 99% copper target and a PVC sample are chosen as representative samples to further explore changes in the plumes due to an increased number of shots per spot as well as to thoroughly characterize the spatio-temporal distribution of emission intensity, excitation (by means of neutral copper Boltzmann plots, in the case of copper, and vibrational temperature of the cyanide molecule, in the case of PVC) and electron density, aiming to adequately characterize and understand the fs-LIP behavior in the present experimental conditions with the purpose of future exploitation in other experimental arrangements (e.g. depth profiling, orthogonal double pulse scheme…) particularly regarding multi-matrix samples.

2. Experimental set-up

The experimental setup includes a Yb:KGW fs-laser (<290 fs, Pharos, Light Conversion), integrated inside a modified ablation unit (NWRFemto UltraCompact, ESI). The unit is fixed to an optical table (RP Reliance, Newport) in order to ensure the preservation of optical alignment. The laser beam can be extracted out of the ablation chamber and is redirected by a set of custom mirrors (CVI Optics) towards a focusing objective (35 mm working distance, model LMH-5×-1064 from Thorlabs). The laser wavelength is the fundamental 1028 nm, and the frequency is set to 10 Hz. Its maximum energy per pulse, 1.5 mJ, is used throughout this work. Spot size is 60 μm (sample surface on the focal plane of the objective), estimating a fluency of 53 J/cm^2 and an irradiance of $1.8{\cdot}10^{14}$ W/cm^2. No significant filamentation-related effects are expected in these conditions.

Light from the plasma plume is directly focused onto the entrance slit of a Czerny-Turner spectrometer with two available diffraction gratings of 1200 and 2400 lines/mm (Andor Technology, Shamrock SR-500i-D1) coupled to an ICCD (Andor Technology, iStar DH334T-18F-E3) via two Ø50.8 mm plano-convex lenses of 100 and 300 mm focal lengths (LA4545-UV and LA4855-UV from Thorlabs, respectively) that result in a 3:1 magnification of the image. The lenses are mounted on a motorized linear stage (Dover Motion) with motion parallel to the spectrometer, allowing for a precise placing of the plasma image so that its vertical axis of symmetry is well-centered over the entrance slit. The spatial resolving power of the experimental set-up is determined using a USAF 1951 resolution test chart, being 32 line pairs per mm (~16 μm). The scale of the images that are acquired with the iCCD is also obtained, corresponding to 4.25 μm/pixel. The spectral response of the detection, characterized with a calibrated Tungsten (Bentham Instruments Limited) lamp utilizing the same optical elements as in the present work (e.g. lenses, gratings, detector), is properly accounted for. Sample positioning is controlled with a motorized stage (Dover Motion) on the XY plane and with a vertical translation stage (MVS010/M, Thorlabs) on the Z direction. The focusing distance is monitored with an optoNCDT 1420 laser-meter from Micro-Epsilon. Except where otherwise stated, data treatment was carried with home-made MATLAB2022a software.

2.1. Fast photography

The entrance slit of the spectrometer was opened to its full aperture (3 mm) and the 1200 lines/mm diffraction grating is centred at 0th order to obtain spectrally integrated images of the plasma plume. Considering the quantum efficiency of the CCD intensifier, as well as the spectral

response of all other relevant elements of the set-up, the wavelengths composing the images are approximately within the 200–800 nm range. According to the lifetime of the plasma in our experimental conditions, fourteen temporal windows were defined (Table 1) covering a range from 10 ns to 15 μs of acquisition delay. The integration times were kept as short as possible in order to obtain more accurate snapshots of the plume evolution, and detector gain was adjusted as necessary to improve SNR.

A set of eight samples (Table 2) was explored at this stage. The reference samples that were used throughout this work, a high-purity copper plate and a PVC plate, were compared to other metals and dielectrics in order to identify potential differences arising from the nature of the matrix being ablated. For the comparison of matrices, four pre-shots were carried out and the following four shots were accumulated. All measurements were done by triplicate. For the purpose of having a more precise reference for the spectrally-resolved measurements on Cu and PVC, the evolution of the plasma plume in these matrices was also studied in different conditions of ablation, namely 40 pre-shots and 40 accumulated shots per spot (from now on named 'reference conditions'); this also allows for a comparison of the plume resulting from different degree of damage on the sample.

2.2. Spectrally resolved images for emission intensity and diagnostics

A thorough study of discreet emission was carried out on copper and PVC. Detection was made utilizing a 100 μm slit aperture and a 1200 lines/mm grating. Acquisition delays were maintained with respect to the previous section in order to correlate information from these measurements with fast photography results, but integration times (Table 3) were increased to improve SNR in the spectral images; the time windows at this stage still did not overlap. When comparing measurements carried out at different integration times and/or gain values, the intensities are corrected by approximating a direct proportion with respect of integration time (given that gate times are kept reasonably short) and by normalizing to the corresponding gain factor (which was previously determined with a continuous light source). As previously stated, forty pre-shots were carried out, followed by forty-shots that were accumulated to obtain a single spectral image.

The excitation temperature diagnostics were carried out through Cu I emission. For this study, three spectral windows containing up to 9 copper lines with known spectroscopic parameters available in NIST database [28] covering a relatively broad range of upper-level energies were chosen as shown in Table 4. Aside from the relevant spectroscopic parameters of the lines, the time intervals in which they could be observed and/or be adequately resolved are also indicated in Table 4. At the latest considered delay (5 μs), only lines 510, 515 and 521 nm could be observed and utilized to build a Boltzmann plot; these three lines are often used for excitation temperature diagnostics in the literature [27,29,30] due to their considerable energy gap and wavelength proximity.

Excitation temperatures were obtained from the well-known Boltzmann plot method given by Eq. (1) [31]:

$$ln\left(\frac{I_{ji}}{A_{ji}g_j}\right) = -\frac{1}{T_{exc}k_B}E_j + ln\left(\frac{FC}{\mathbb{Z}(T)}\right) \quad (1)$$

where I_{ji} is the line intensity (corrected by instrumental sensitivity at the corresponding wavelength), A_{ji} is the transition probability, g_j is the degeneracy of the upper-level involved in the transition, T_{exc} is the excitation temperature, k_B is the Boltzmann constant, E_j is the upper-level energy, F is an experimental factor, C is the relative molar concentration of the considered species (Cu I) and $\mathbb{Z}$ is the partition function at the given excitation temperature.

Various species of neutral, ionic and molecular nature were also selected to explore the emission distribution in the PVC plasma. These are summarized in Table 5, where the spectroscopical information of atomic and ionic lines has been taken from NIST Atomic Spectra Database (atomic and ionic lines) [28] and information about the molecular emitting species, from Pearse and Gaydon (1976) [32]. The CN experimental emission was fitted to simulated spectra by means of LIFBASE software [33], in which rotational and vibrational temperature were explored with a coarse resolution of 100 K.

Table 2
Composition of the eight studied samples. *The PTFE and the PVC samples contain an undetermined amount of Ca (detected on the surface and in bulk, respectively).

Sample	CRM	Main components (%)	Other (%)
Cu (ref)	–	Cu > 99.9	–
Zn	SRM 628	Zn: 94.657	Al: 4.950, Cu: 0.611
Brass	31×-7835.4	Cu: 67.130, Zn: 30.360	Pb: 1.049, Al: 0.525
Fe alloy	13×-NSD1	Fe: 49.091, Mn: 23.530, Cr: 24.510	Mo: 1.120
Ni alloy	BS 625 B	Ni: 59.820, Cr: 21.285, Mo: 9.583, Fe: 4.511	Al: 0.332, Cu: 0.225
Mg	68×-MGH6	Mg: 98.093	Al: 0.230
PTFE	–	$(C_2F_4)_n$	*Ca
PVC	–	$(C_2H_3Cl)_n$	*Ca

2.3. Electron number density evaluation

The Cu I line at 515.32 nm was utilized to study the electron number density in the Cu plasma. Due to its moderate Stark broadening, a slit aperture of 70 μm and the 2400 grooves/mm diffraction grating were utilized (covering a 507.2–526.8 nm range). Acquisition was made with the same temporal parameters stated in Table 3. The instrumental broadening was measured with an Ar-Hg lamp and was determined to be a Voigt-shaped profile with a Gaussian width of 0.19 Å and a Lorentzian width of 0.36 Å at the considered wavelength. Consequently, the copper line was fitted to a Voigt profile with a fixed gaussian width equal to the instrumental broadening (using the built-in function of Origin 8.5 software). The Stark component of the broadening was then obtained by subtracting the corresponding instrumental broadening from the computed Lorentzian width. Electron density was finally calculated, assuming that collisions with ions were negligible, according to Eq. (2) [34]:

$$\Delta\lambda_{FWHM}^{Stark} = 2\omega\left(\frac{N_e}{N_e^{ref}}\right) \quad (2)$$

where ω is the electron impact parameter of the transition, given for a reference electron density. The broadening parameter for the studied line (FWHM = 1.9 Å) was taken from [35], where it is given with accuracy of 30–50% for a temperature of 10,000 K and an electron number density of 10^{17} cm^{-3}.

The results from excitation temperature and electron number density diagnostic studies in the copper plume were used to obtain the ionic-

Table 1
Acquisition windows for spectrally integrated measurements. Note that delay time could be set with a precision in the order of nanoseconds; decimal places of longer delays were omitted for clarity.

Delay (μs)	0.010	0.05	0.1	0.2	0.3	0.5	0.75	1	1.5	2	2.5	5	10	15
Gate (μs)	0.005		0.025			0.05			0.1		0.25		0.5	

Table 3
Acquisition windows for spectrally resolved measurements.

Delay (μs)	0.01	0.05	0.1	0.2	0.3	0.5	0.75	1	1.5	2	2.5	5
Gate (μs)	0.01		0.05			0.1			0.2		0.5	1

Table 4
Spectroscopic parameters of the utilized lines obtained from NIST database.

Spectral window (nm)	Line (nm)	A_{ji} ($\cdot 10^7$ s^{-1})	g_j	E_j (eV)	Time interval (ns)
450–470	453.08	0.84	2	6.552	300–1000
	453.97	2.12	4	7.883	
	458.70	3.2	6	7.805	50–1000
	465.11	3.8	8	7.737	
507.2–526.75	510.55	0.2	4	3.817	
	515.32	6.0	4	6.191	50–5000
	521.82	7.5	6	6.192	
565.4–584.5	570.02	0.024	4	3.817	50–2500
	578.21	0.165	2	3.786	

Table 5
Studied atomic, ionic and molecular species in PVC plasma.

Spectral window (nm)	Species	Signals	Time interval (ns)
377.8–398.2	CN	Violet system, $B^2\Sigma - X^2\Sigma$ ($\Delta v = 0$)	50–2000
	Ca II	Doublet 393.37 and 396.84 nm, with upper-level energies 3.151 and 3.123 eV, resp.	50–1000
510.2–529.75	C_2	Swan system, $A^3\Pi_g - X'^3\Pi_u$ ($\Delta v = 0$)	50–2000
	Ca I	Multiplet (526.17, 526.21, 526.42, 526.56 and 527.03 nm) with $E_j \sim$ 4.877 eV	50–750
583.5–602.45	Na I	Doublet 589.00 and 589.59 nm, with E_j = 2.104 and 2.102 eV, resp.	50–5000
	CaCl	Orange system $B^2\Sigma - X^2\Sigma$ ($\Delta v = 0$)	50–5000
647–665.5	H I	Balmer α (656.28 nm), with E_j = 12.088 eV	50–200

neutral Cu ratio ($N_{Cu\ II}/N_{Cu\ I}$) via the Saha equation (Eq. (3)) [34]:

$$\frac{FC(Cu\ II)}{FC(Cu\ I)} \approx \frac{N_{Cu\ II}}{N_{Cu\ I}} = \frac{1}{N_e} 2 \cdot \frac{\mathbb{Z}_{Cu\ II}(T)}{\mathbb{Z}_{Cu\ I}(T)} \cdot \left(\frac{2\pi m_e k_B T_{ion}}{h^2}\right)^{\frac{3}{2}} e^{-\frac{E_{ion} - \Delta E_{ion}}{k_B T_{ion}}} \quad (3)$$

where $\mathbb{Z}_{Cu\ I/II}(T)$ are the partition functions, obtained from NIST [28], for ionic and neutral copper, E_{ion} is the ionization potential of copper and ΔE_{ion} is the Debye shielding correction.

On the other hand, emission from the Hα line was used to estimate the electron density in the PVC plasma. Measurements were carried out as described in Section 2.2 (Table 4), for which the instrumental broadening was contributed by a Gaussian width of 0.6 Å and a Lorentzian width of 0.7 Å (at the considered wavelength). The Stark component was obtained as described for copper and corresponded to an electron density relying on Gigosos and Cardeñoso's database [36].

3. Results and discussion

3.1. General behavior of the plasma plumes for different matrices

The evolution of the plasma plumes induced on each of the 8 samples is shown in Fig. 1, where each of the images has been normalized to the maximum intensity in the spectral window after subtracting the value of counts attributed to reading noise, which was obtained as an average of the signal from pixels not illuminated by the plume. It can be pointed out that most of these plumes are characterized by a two emitting component structure, as previously stated and in agreement to the literature [18,19,21,37]. In the present work, a higher component quickly moving upwards is always present and dominates intensity-wise at the early stages of evolution (≲1 μs) regardless of sample nature (metallic or dielectric), whereas a slow component remains near the sample surface (<0.5 mm) throughout the plume evolution, undergoing a radial expansion while remaining otherwise stationary.

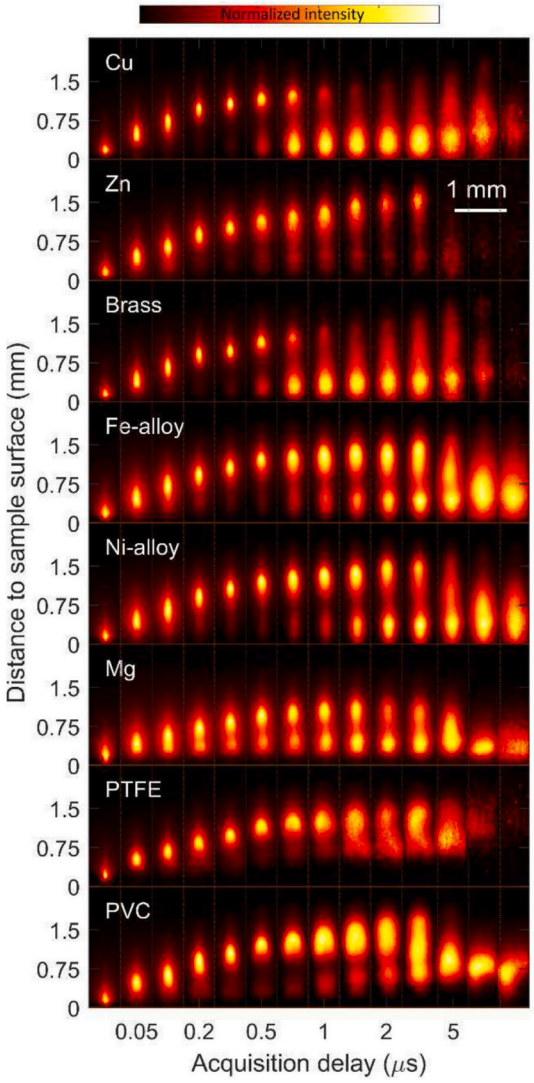

Fig. 1. Temporal evolution of the plasma plume for each of the 8 samples.

Moreover, if focusing on the dielectric samples, it can be seen that PTFE does not present a clearly separated slow component, whose lack was explicitly pointed out in the literature for a sample of silica [19] as opposed to various metals [17]. However, PVC appears to have a similar structure to metallic samples. This seemingly slow feature is only apparent for the first superficial shots, whereas analogous measurements performed in so-called reference conditions (40 accumulated shots, after an equal number of pre-shots) reveal an isolated fast component without any accompanying emitting component in the lower region. The copper plasma maintains the same structure as in Fig. 1 despite the significantly greater number of shots and, in fact, the lower component very slightly increases its relative importance, intensity-

wise. A Figure depicting the evolution of the Cu and PVC plumes in reference conditions is available in Supplementary material (Supp. Fig. 1.a-b). It can additionally be noted that lowering the laser fluence also resulted in a decrease of the upper component brightness and the extent of its vertical displacement, as illustrated with the copper sample in Supp. Fig. 2. Similar results were reported by Anoop et al. in vacuum [24] and by Zhang et al. in atmospheric air, both experimentally and by plasma modelling [25].

Another feature that distinguishes the plumes in Fig. 1 is the expansion dimension. While metallic matrices (Cu, Zn, brass, Fe- and Ni-alloys) are characterized by an elongated expansion (one dimensional) of the fast component, a radial expansion becomes evident (three dimensional) in PTFE and PVC. This is also clearly observed in Supp. Fig. 1. Interestingly, the Mg plume also presents a radial growth of the fast component, which also moves at a lower speed, barely reaching 1 mm of distance from the sample surface. On the contrary, the upper component of the Zn plume displaces further than those of any other matrix, reaching up to 1.5 mm.

The differences in the behavior of the fast component can be quantified by monitoring the position of the maximum intensity with respect to the delay time. This is shown in Fig. 2 for six matrices, omitting brass (which is analogous to copper) and the Ni-alloy (analogous to the Fe-alloy). The fittings of the fast component displacement of all matrices, including reference conditions, are available as Supplementary material (Supp. Figs. 3 and 4a-b). The perpendicular displacement was modelled according to two regimes of evolution. The initial propagation ($t < 200$ ns) is well modelled by a blast wave model (point explosion), as given by Eq. (4)

$$d(t) = \alpha(\xi)\cdot t^{2/(2+\xi)} \quad (4)$$

where $\alpha(\xi)$ comprises various experimental parameters (namely the density of the surrounding gas and the fraction of laser pulse energy that takes place into the plasma state conversion) and ξ is a dimension factor (1 for a one-dimensional expansion, 2 for a cylindrical expansion, and 3 for a spherical expansion) [8]. All matrices except Mg, PTFE and PVC are well described by a linear propagation ($\propto t^{2/3}$), while the former are better described by a spherical propagation ($\propto t^{2/5}$). This is coherent with the evolutions observed in Fig. 1, as the component in these three matrices appear to be rounder (radially expanded) than the rest. Afterwards, the displacement is notably slowed down due to the increased collisions with background gas and can be described by the drag model, as given by Eq. (5).

$$d(t) = d_{max}(1 - exp(-\beta t)) + d_0 \quad (5)$$

where β is the slowing coefficient [38,39], d_0 accounts for the position of the component when the change of regime occurs and d_{max} is the maximum distance travelled afterwards.

Additionally, the displacement speed was estimated for all samples, obtaining initial values between ~6 km/s (Mg) and ~ 8 km/s (PTFE and PVC).

The fitting parameters for all matrices are shown in Table 6 with their corresponding uncertainties. It is interesting to note that the slowing coefficient of Zn is notably lower (1.7 ± 0.9 μs^{-1}) than the average value of all samples ablated in analogous conditions whether Zn itself is included (4.0 ± 1.2 μs^{-1}) or excluded (4.4 ± 0.8 μs^{-1}) from the computation. The reason why the fast component of Zn continues displacing at a higher speed for a longer time is not clear and will be object of study in a future work. On the other hand, the $\alpha(\xi)$ coefficient of the blast wave model is similar for most metals ablated in analogous

Table 6
Coefficients of the fits from Fig. 2. The initial expansion of samples marked with * are better described by a spherical shockwave ($\xi = 3$) rather than planar ($\xi = 1$).

	Blast wave model		Drag force model			
Sample	$\alpha(\xi)$ (mm·μs$^{-2/(2+\xi)}$)	R^2	d_{max} (mm)	β (μs^{-1})	d_0 (mm)	R^2
Cu	3.4 ± 0.5	0.988	0.9 ± 0.3	6 ± 3	0.3 ± 0.3	0.987
Zn	3.1 ± 0.6	0.979	0.92 ± 0.17	1.7 ± 0.9	0.58 ± 0.19	0.957
Brass	3.0 ± 0.2	0.996	1.0 ± 0.2	4.9 ± 1.8	0.3 ± 0.2	0.990
Fe-alloy	3.3 ± 0.6	0.978	0.92 ± 0.19	4.0 ± 1.3	0.4 ± 0.2	0.977
Ni-alloy	3.1 ± 0.4	0.992	1.0 ± 0.2	3.6 ± 1.5	0.4 ± 0.2	0.964
Mg*	1.43 ± 0.09	0.996	0.74 ± 0.03	4.0 ± 0.3	0.33 ± 0.03	0.999
PTFE*	1.72 ± 0.16	0.992	0.91 ± 0.09	4.0 ± 0.7	0.38 ± 0.10	0.995
PVC*	1.5 ± 0.4	0.949	1.11 ± 0.11	4.1 ± 0.7	0.23 ± 0.12	0.995
Cu (ref.)	2.1 ± 0.7	0.961	0.79 ± 0.14	4.3 ± 1.5	0.21 ± 0.16	0.992
PVC (ref)*	1.5 ± 0.4	0.949	0.99 ± 0.15	6.1 ± 1.3	0.08 ± 0.16	0.997

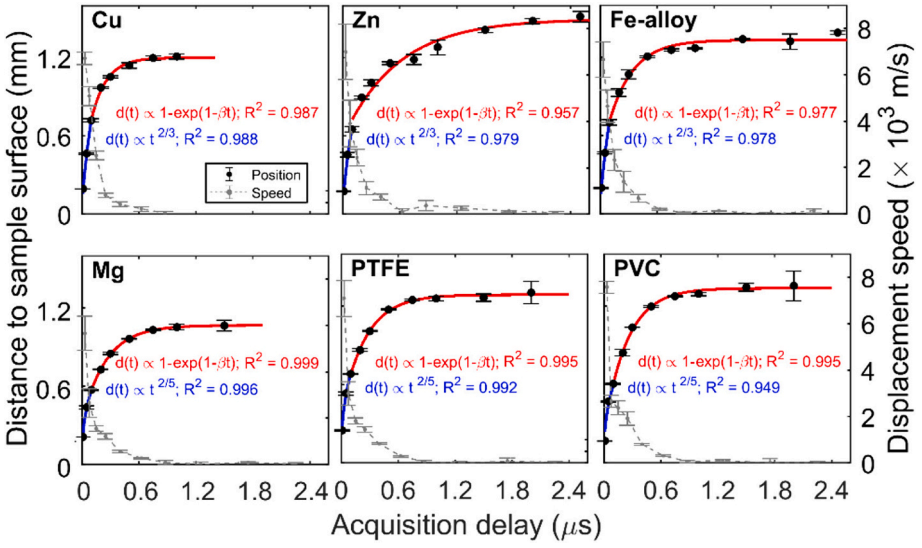

Fig. 2. Displacement of the fast component for six matrices.

conditions, averaging to $\alpha(\xi) = 3.3 \pm 0.2$ mm·μs$^{-2/3}$), suggesting similar deposition of energy in all cases. The samples better described by the spherical propagation, on the other side, have an average $\alpha(\xi)$ coefficient of 1.55 ± 0.15 mm·μs$^{-2/5}$.

If we compare the evolution of Cu and PVC plasma in both studied conditions, it can be pointed out that in both cases initial speed is lower (5.0 ± 0.1 and 6.5 ± 0.4 km/s, resp.) than what is obtained for fewer shots (6.7 ± 0.3 and 7.6 ± 0.3 km/s, resp.). In the case of Cu, fast component displaced up to 1 mm of height rather than up to 1.2 mm. Moreover, the $\alpha(\xi)$ coefficient is slightly lower (2.1 ± 0.7 mm·μs$^{-2/3}$), which could be explained by a less efficient laser energy deposition when ablating over a deeper crater, as interaction with the walls as well as defocusing will occur to an extent (ablation rate on the copper sample was roughly estimated to be 1 μm/shot from the complete drilling of a 100 μm thick copper sheet with 100 laser shots). However, both the $\alpha(\xi)$ coefficient and the maximum distance to sample surface remain practically unchanged in the dielectric sample. Within uncertainty, β coefficients for both samples are compatible with the previous results.

3.2. Spectrally resolved emission intensity of Cu plasma

Emission from the copper plasma was further studied with spatial and spectral resolution. Fig. 3.a shows the spatially resolved spectra from the copper plasma preserving the spatial resolution along the entrance slit for three given acquisition delay times, while Fig. 3.b shows the manually integrated spectra in order to illustrate the time-evolving broadening of the lines. At the earliest delay at which a measurement was performed (10 ns) no discreet emission is observed, but rather a continuous emission localized very close to the sample surface. Afterwards, discreet emissions completely dominate the spectral windows.

The intensity distribution along the entrance slit of four representative Cu I lines (Table 4), chosen to illustrate various upper-level energies, as well as continuum emission (intensity from a spectral region lacking discreet emission, after reading-noise subtraction) is shown in Fig. 4.a-e. For each case and acquisition delay, a normalization of the intensity profile was carried out. For all discreet lines, differentiated upper and lower components at coherent spatial positions can be pointed out.

If emission distributions of the lines under study are compared, after the fast initial expansion (>0.2 μs), the transitions arising from the lower laying multiplet $[3d^{10}4p]^2P_{1/2,3/2}$ (510.55 and 578.21 nm, as well as 570.02 nm, not shown here) behave analogously: intensities in the upper and lower components remain comparable throughout the plasma plume evolution (Fig. 4.a. and 4.c.). On the other hand, transitions involving the intermediate upper-level energies $[3d^{10}4d]^2D_{3/2,5/2}$ (515.32 nm, Fig. 4.b. and 521.82 nm, omitted) are roughly 50% brighter in the upper component, with an outlier at a time delay of 1.5 μs, in which they become comparable. Finally, deexcitation from the higher upper-level energies (458.70 nm, in Fig. 4.d, as well as all other lines detected in the corresponding spectral window) is remarkably localized within the upper component up until it cannot longer be detected (>1 μs). This qualitative analysis suggests lower temperatures in the slow component. Moreover, given that the highest levels are prone to be populated through recombination processes, the ionization degree of the upper component could also be higher.

On the other hand, the continuum emission (Fig. 4.e) shows an evolution quite analogous to what is seen in the fast photography images (profiles shown in Fig. 4.f), with a switch of maximum intensity position from the top to the bottom component at 0.75–1 μs. This behavior is not seen for any of the considered discreet lines. Increased continuum emission is expected in presence of hot nanoparticles, which are known to be present near the sample surface for metallic targets, such as copper, and favored at higher fluences (> 1 J/cm^2) at the expense of less atomized matter [17,18,40]. Hence, the relative predominance of continuum in the lower component at later stages of the plasma evolution could be attributed to nanoparticles being present only in that region of the plume. Note that contour plots analogous to Fig. 4.f build from the plume images shown in Fig. 1 are also available in the Supplementary material (Supp. Fig. 5).

In order to quantify the apparent differences in excitation, two spatial regions (shown overlayed in Fig. 4.a-f) are defined. Both are set to cover a total height of 255 μm (60 iCCD pixels). The bottom one comprises the slow component in an almost static spatial interval (white dotted lines), whereas a steeply varying position is set at each time for the fast component (black dotted lines). It is considered that the two distinct components are defined from 200 ns onwards, whereas they overlap at earlier stages. By summing the intensity of the regions, a single spectrum is obtained in each region for each acquisition delay. The shape of the spectral lines was attributed to the convolution of Stark (Lorentzian) and instrumental broadening, neglecting other sources of broadening. The resulting convoluted profile was considered to be a Voigt profile, and all emission lines seen in the spectra were fitted to

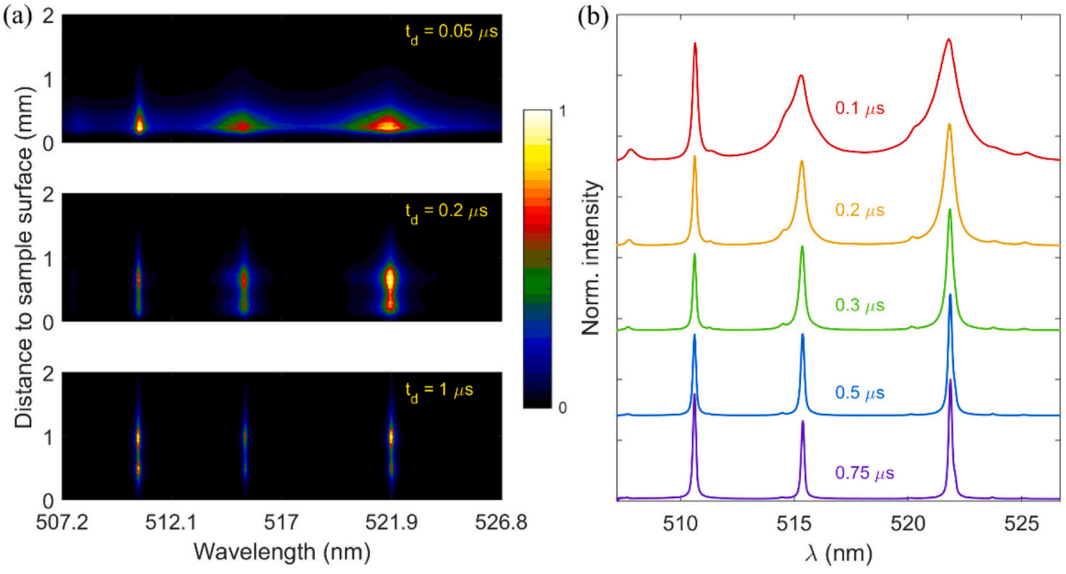

Fig. 3. (a) Three examples of spatially- and spectrally-resolved measurements and (b) five examples of spectra after manually integrating along the entrance slit corresponding to copper plasma emission. All spectra are individually normalized.

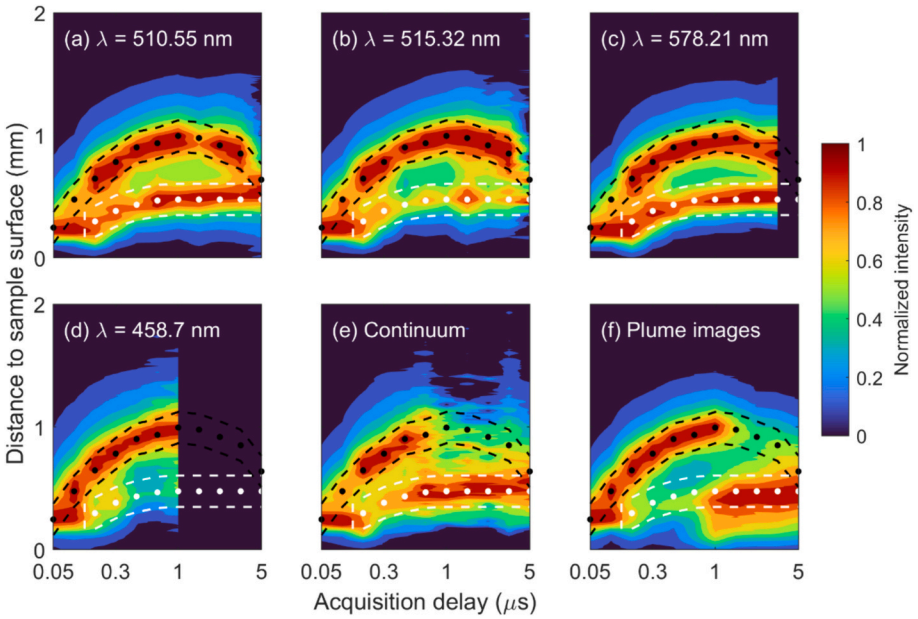

Fig. 4. Contour plots (level step = 0.1) of the intensity distribution from Cu I lines at (a) 510.55, (b) 515.32, (c) 578.21 and (d) 458.7 nm, from (e) continuum emission and from (f) spectrally integrated images. Note that, for visualization purposes, the x-scale is not linear. The spatial ranges used for intensity integration of the upper and lower components are shown overlayed.

pseudo-Voigt profiles to obtain the line areas of interest free of spectral interferences.

The computed intensity decays of the example Cu I emission lines are plotted in Fig. 5.a-d for each component of the plasma plume. The values have been normalized to integration time and detector gain. The relative uncertainties of the areas are typically <10%. As expected, lines 510.55 and 515.32 nm are the most persistent in time. The temporal decay of the former is, of course, very similar to that of line 578.21 nm. Moreover, the corresponding intensities in the fast and slow components are consistent, indicating that the $[3d^{10}4p]^2P_{1/2,3/2}$ levels are being similarly populated in either component. On the other hand, the intensity of transition 515.32 nm remains higher in the upper component throughout the plasma evolution (minus the anomalous point at 1.5 μs and the value at 5 μs, where the two components are no longer clearly distinguishable) but the deexcitation rate is analogous. Finally, the 458.70 nm shows the greater discrepancy among plasma regions not only in terms of relative intensity but also regarding the deexcitation rate, which appears to be quicker in the lower component, suggesting that potential repopulation mechanisms of the involved upper-level (e.g. collisions and recombination processes) are not as efficient in that region.

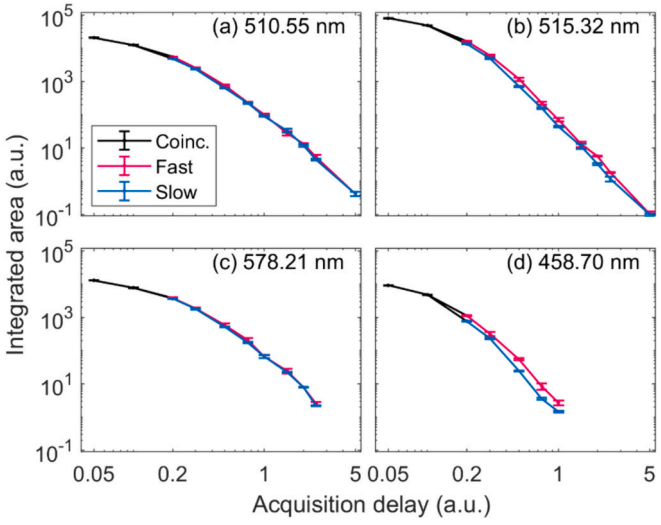

Fig. 5. Decay of integrated intensities, at each component, of Cu I lines (a) 510.55, (b) 515.32, (c) 578.21 and (d) 458.70 nm. Note that all plots cover the same x, y intervals for ease of comparison. Continuous lines serve as a guide to the eye.

3.3. Excitation conditions in the components of the Cu plasma

The results obtained from the Boltzmann plots (available in Supp. Figs. 6-8) indicate that excitation temperatures in the fast component are indeed higher than in the slow component throughout the 200–5000 ns dataset. Moreover, the temporal evolution was well fitted to a power decay model of the form $T \propto t^{-b}$ (Fig. 6.a) for the purpose of quantifying the observed difference. In the ideal case of an adiabatic expansion of a plasma expanding in vacuum, the coefficient b equals 2; a slower decay (b = 1) is expected when excitation is sustained by three-body recombination processes that result in the population of the higher-laying levels of the neutral species [41,42]. Slower deexcitation than either of those models has been reported in works dealing with femtosecond ablation in ambient air [8,29,30,43,44]. The fitting of the experimental data in the present work resulted in moderately increased deexcitation of the slow component (b = 0.98 ± 0.09), which was 32 ± 11% greater than the value obtained for the fast component (0.66 ± 0.09). Although the decay of the slow component approaches the case sustained by recombination, this scenario requires a high degree of ionization, and fs ablation experiments have generally shown the opposite [45,46].

Electron densities were determined to be analogous for the upper and lower components throughout the whole temporal range that was analysed (Fig. 6.b). The decay could also be modelled by a power decay model, $n_e \propto t^{-b}$, with a decay constant of 1.67 ± 0.09. This value was computed separately for each component and the value given here is the average of the two, with the total uncertainty propagated taking into account both the statistical deviation of the mean as well as the individual uncertainties given by the fitting procedure in each case. At the earliest considered time, electron number density in the not-yet-split plume is approximately $7{\cdot}10^{17}$ cm^{-3} and decreases in two orders of magnitude after 1 μs, to $9{\cdot}10^{15}$ cm^{-3}. The decay constant is higher than

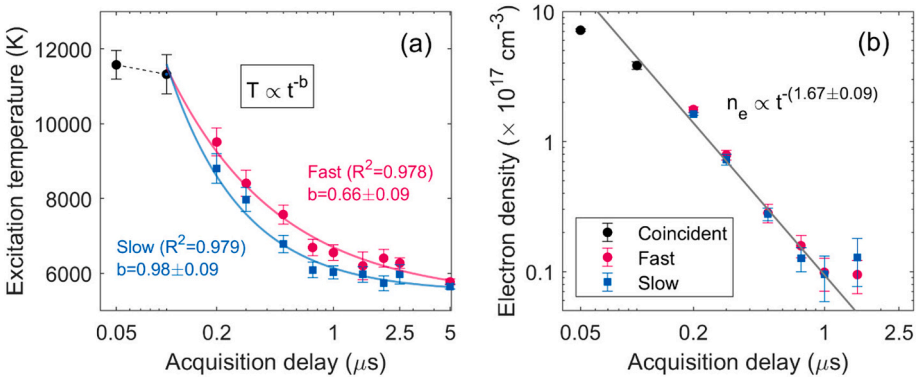

Fig. 6. Temporal evolution of (a) excitation temperature and (b) electron density in each component.

other reported values [8,29,30,43,44], albeit still reduced with respect to what would be expected from an adiabatic expansion (b = 3) [42].

As a necessary, although not sufficient, requirement to ensure LTE, the McWhirter criterion [47] was applied to evaluate if the electron density in the plasma is high enough to allow the dominance of collisional processes given the calculated excitation temperatures. The largest energy gap of the considered transitions was utilized to compute these values, which were the same (within uncertainties) for both components and varied between $2.5{\cdot}10^{15}$ and $1.8{\cdot}10^{15}$ cm^{-3} from 50 ns to 1 μs, consistently lower than the determined values of Fig. 6.b.

It is also possible to estimate the neutral copper density in both components from the Boltzmann plots, given that the spatial regions are equally sized and an equal F factor in the intercepts can be assumed (see Eq. (1)). The subsequent analysis is done with caution, as the relative uncertainties of the FC values are considerable (30%) and uncertainty intervals from both components overlap significantly, but results suggest that the density of neutral atoms is similar (see Fig. 7.a.) in both components. Hence, the extent of excitation, rather than the number of Cu I atoms present in each component, seems to be responsible for the different intensity in the components. Of course, it must be noted that ionic copper is not being accounted for when comparing the population of each component. The ratios of total copper densities might be different particularly considering that, under the LTE conditions that are being assumed, higher excitation temperature implies an equally higher ionization temperature. To explore this, the degree of ionization was evaluated through the Saha equation (Eq. (3)), considering the previously obtained excitation temperatures and the electron number densities. The obtained ionic-to-neutral ratios are shown in Fig. 7.b., highlighting the increased ionic-to-neutral ratio in the fast component. However, in agreement with the previously mentioned literature [45,46], the ionization degree is very low overall, with ionic population being moderately larger than its neutral counterpart only at delay times <200 ns, approaching a 10% of ionization degree at a delay time of 500 ns.

3.4. Spectrally resolved emission intensity of PVC plasma

The PVC plasma was analysed in a similar fashion. Intensity profiles along the entrance slit were obtained for all measurements (plasma plume and the various analyte signals), normalized at each acquisition time and arranged as contour plots depicting their qualitative distribution (Fig. 8.a-h). The plume profiles present a well-defined single component (Fig. 8.a), for which a 255 μm-wide region centred on its maximum emission intensity position has been noted with white markings. These are maintained in the remaining plots for the sake of an accurate spatial comparison. Continuum emission (Fig. 8.b), obtained analogously as for copper plasma, very strongly resembles the former distribution with no outstanding features. Highest emission intensity of most species considered (Fig. 8.c,e-g, corresponding to CN, C_2, Ca I and Na I, respectively) is within the limits of the defined region, with moderate discrepancies arising at longer delays at which the dynamics of the plume become chaotic and plasma-shape reproducibility is significantly worsened. On the contrary, a notable spatial separation can be pointed out for Ca II (Fig. 8.d) and CaCl (Fig. 8.h) at the early stages of the plasma evolution. Their respective maximum emission positions (black dots) are separated by as much as 370 μm. The distribution of ionic calcium is consistently localized at a moderately higher distance from the sample surface (note that this signal belongs to the same spectral window as CN, which lacks such a systematic discrepancy). The halogenated molecule, on the other hand, switches from emitting mainly from the tail of the plasma plume component to extending all over it, possibly due to recombination of neutral Ca and Cl atoms becoming

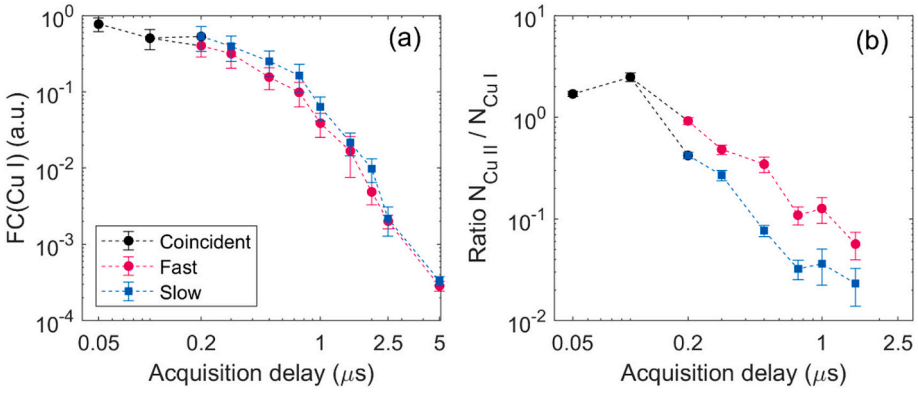

Fig. 7. Evolution, in each component, of the (a) neutral copper density estimated from the Boltzmann plots and (b) ionic/neutral ratios calculated with the previously determined excitation temperatures and electron densities.

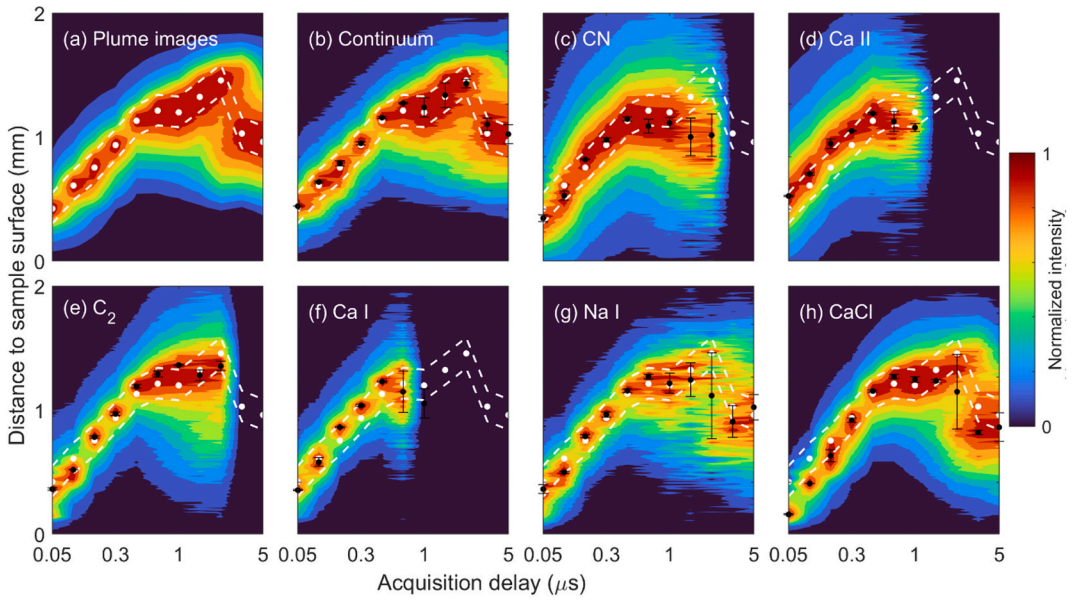

Fig. 8. Contour plots (level step = 0.1) of intensity distribution of PVC plume, corresponding to (a) spectrally non-resolved emission, (b) continuum, (c) CN violet system, (d) resonant Ca II emission, (e) C_2 swan system, (f) Ca I multiplet, (g) orange Na I doublet and h) CaCl orange system. Note that, for visualization purposes, the x-scale is not linear. (For interpretation of the references to colour in this figure legend, the reader is referred to the web version of this article.)

widespread as the plasma cools down. In order to further emphasize this difference, Fig. 9 includes the maximum emission position for Ca II and CaCl, as well as CN and Na I as emission references from their respective spectral windows. These are shown overlayed to the plasma plume distribution to aid visualization. This separation suggests that, despite the plasma consisting of a single component, this does not present a homogeneously distributed population and/or excitation. Notably, all molecular species (CN, C_2 and CaCl) were seen in the earliest time-window (covering the 50–100 ns interval), even if not dominant over the nearby atomic or ionic emission.

3.5. Excitation conditions in the PVC plasma

The atomic emission in the PVC plasma is rather poor to build a Boltzmann plot out of any element, and self-absorption was apparent on the Ca II doublet, since the intensity ratio deviated from the theoretically expected given their transition probabilities and degeneracies. As an alternative approach, the cyanide violet B-X system (sequence $\Delta v = 0$) was utilized to compute rotational temperatures. Emission in the 377.8–398.2 nm spectral window was spatially integrated following a similar procedure as explained for the Cu sample, obtaining a spectrum per acquisition time. Prior to fitting the molecular signal to a synthetic spectrum generated using LIFBASE, the slightly interfering (at 50–100 ns delay times) emission from Ca II was fitted to pseudo-Voigt profiles and subtracted, and the molecular emission was corrected to the instrumental response of the system to prevent any distortion in the molecular bands intensity ratios. A Voigt instrumental profile, with a total width of 1.48 Å, was chosen in the fitting software. Vibrational and rotational temperatures were individually (this is, without assuming LTE) explored with a resolution of 100 K until the experimental spectrum was well reproduced. Three representative examples of experimental and simulated emission can be found in Supp. Fig. 9.

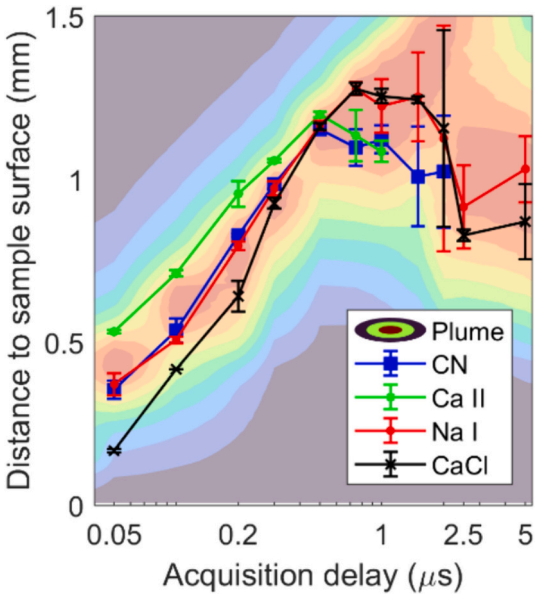

Fig. 9. Position of maximum intensity of (a) CN, (b) Ca II doublet, (c) Na I doublet and (d) CaCl overlayed to the plume intensity contour plot.

Correlation coefficients were $R^2 > 0.991$ between 100 and 750 ns, and $R^2 > 0.977$ for the earliest and latest acquisition windows in which SNR of the molecular system was lower. The resulting vibrational temperatures (Fig. 10.a) illustrate a slow decay, well described by a $T_{vib} \propto t^{-0.17 \pm 0.02}$ function. This is a considerably slower decrease than what was seen for the excitation temperature in copper plasma, although the temperatures are overall lower from the beginning (9600 ± 400 K) to the latest acquisition delay in which SNR was high enough to model the molecular emission (5900 ± 200 K). The uncertainty of the parameters was propagated considering both the temperature resolution of the fitting and the averaging of three repetitions. On the other hand, the rotational temperatures resulting from the best fit were consistently lower than their vibrational counterpart, varying between 4200 ± 300 K and 5900 ± 120 K, evidencing a lack of thermalization. It must also be pointed out that rotational structure is not well-resolved in the present spectra, compromising rotational temperature accuracy, although lower rotational than vibrational temperatures have been reported in femtosecond ablation of organic matrices from temporally integrated spectra [48].

Taking advantage of the prominent Hα emission present at the beginning of the plasma evolution (Fig. 11), Stark broadening of the line

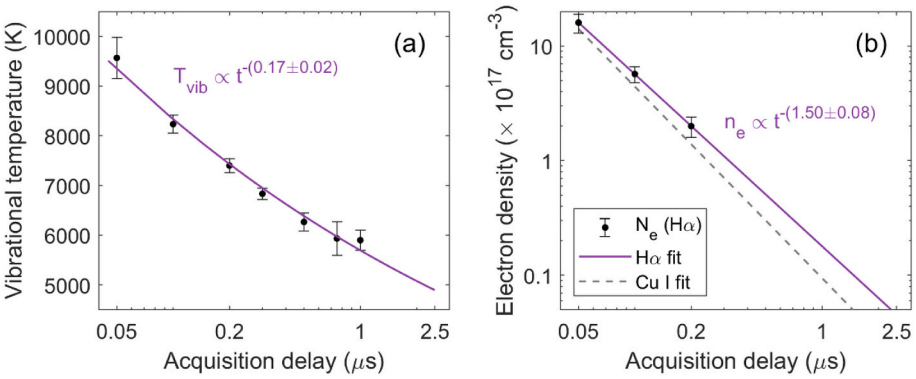

Fig. 10. Temporal evolution of (a) vibrational temperature (CN molecule simulation) and (b) electron density derived from Hα broadening (PVC plasma) compared to results obtained from Cu I (copper plasma).

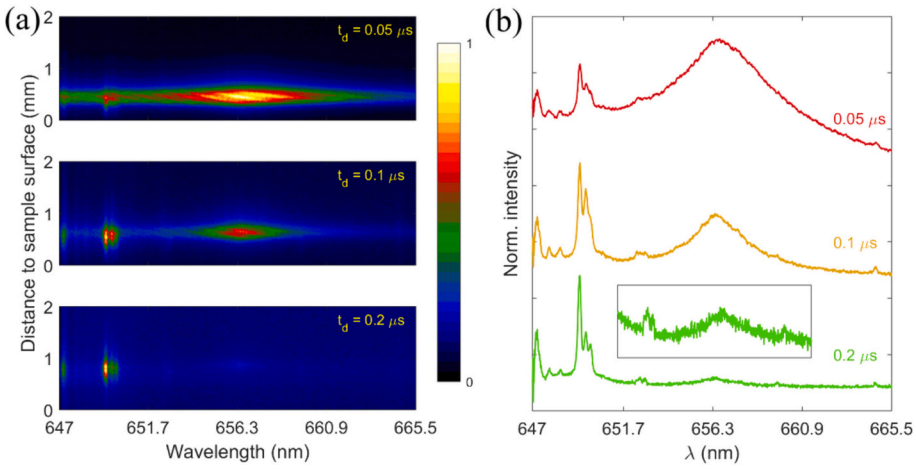

Fig. 11. (a) Spatially- and spectrally-resolved emission of Hα and (b) spatially-ntegrated emission.

could be determined by means of Voigt fitting the spatially-integrated emission in the 50 to 200 ns time windows. The electron number density (Fig. 10.b.) decayed at a marginally lower rate than in the copper plasma (dotted line), with $n_e \propto t^{-1.50\pm0.08}$. The initial N_e doubled the value obtained at an equivalent delay time in the copper plasma. Considering the similarity of excitation conditions in the dielectric and the metallic plumes, the absence of analogous Hα emission in the latter might be due to inefficient incorporation into the plume which, together with the considerable broadening of the line, make it indistinguishable from background emission.

4. Conclusions

A thorough characterization of a femtosecond-laser induced plasma has been carried out in this work. The fast photography measurements of plasma plumes generated on different matrices generally show a clear two-component structure after ~200 ns from the laser shot, with part of the plume evolving close to the sample surface and the remaining, brighter fraction quickly displacing upwards with initial speeds of several km/s. An exception to the clear two-component structure was PTFE, in which only the fast component was evident. The second dielectric matrix studied in this work, PVC, appeared to show a more obvious slow component that, upon further investigation, was seen to appear only for a reduced number of shots. Both matrices were similar regarding the behavior of the fast component in terms of speed and increased radial expansion as opposed to the linear expansion seen for all metallic matrices except Mg. A slightly slower initial velocity was observed when increasing the number of shots per spot both for the copper and PVC matrices, which could be attributed to drilling effects. The consistency of the plasma plume shape could be advantageous for applications and pure Zn and Mg matrices will be further investigated in subsequent works to understand their differing behavior, as no properties of the samples could be reliably identified as cause.

The spatially resolved spectroscopical analysis done on a copper sample utilizing Cu I emission allowed the exploration of excitation conditions in each component of the metallic plasma plume both qualitatively and quantitatively. The relative intensity corresponding to transitions arising from different upper-level energies provided consistent evidence of higher excitation in the fast component, which were then confirmed by means of Boltzmann plot procedure. Electron number density was evaluated from the Stark broadening of Cu I emission line at 515.32 nm and, on the contrary, was determined to be equal in both components within our experimental precision. Neutral copper density was also determined to be comparable in the fast and slow components. However, the ionic-to-neutral copper was seen to be consistently higher in the fast component, although the ionization degree was overall low, as often seen for fs-plasmas. The population differences between the components, albeit generalized, are not drastic.

The analogous study carried out on PVC revealed a certain degree of inhomogeneity in the population distribution of the single component, particularly regarding ionic calcium and molecular calcium chloride emission, which were clearly separated at the front and the tail of the plasma plume at the early stages of evolution whereas all other species (Ca I, Na I, CN, C_2) maximized their emission at a similar position than that of the general plasma plume emission. The violet B-X system of cyanide was utilized to estimate the temperature of the plasma via the

vibrational temperature of the molecule, which was determined to be moderately lower than that of the copper plasma but also to decay much slower. On the contrary, electron density obtained from the Hα broadening (native component of the matrix) was slightly higher, but within the same order of magnitude, than that of the copper plasma and the decay was practically analogous.

The parallel studies carried out in different matrices can be useful in the context of multi-matrix samples, such as printed circuit boards, especially if the spatial distribution of matter and emitters is important as is the case of orthogonal double-pulse systems or detection arrangements which require to limit the studied region for the sake of increasing operating frequency (as fs-lasers can be easily operated in the kHz). In this sense, it is first seen that even for metallic samples notable differences in the extent of the plume expansion can take place, with the most extreme cases being Mg (closest to the sample surface and more radially expanded) and Zn (furthest). Hence, the optimum detection region suffers considerable variation and optimization of an orthogonal re-excitation set-up cannot be easily done simultaneously for a variety of materials. In the case of dielectrics, it is seen that there is some presence of matter in the bottom region of the plume for a small number of shots (PVC) whereas it is concentrated in a single component after an increased number of shots. However, considering the mechanisms in femtosecond ablation, it should also be considered that lower emitting regions are not necessarily depleted of ablated matter. In this sense, absorption and shadowgraphy experiments could be of interest to gain further insight.

CRediT authorship contribution statement

Cristina Méndez-López: Conceptualization, Methodology, Investigation, Formal analysis, Visualization, Writing – original draft, Writing – review & editing. **Cristina González-Gago:** Supervision, Writing – review & editing. **Jorge Pisonero:** Conceptualization, Supervision, Writing – review & editing, Funding acquisition. **Nerea Bordel:** Conceptualization, Supervision, Writing – review & editing, Funding acquisition.

Declaration of competing interest

The author is an Editorial Board Member/Editor-in-Chief/Associate Editor/Guest Editor for [Journal name] and was not involved in the editorial review or the decision to publish this article.

Data availability

Data will be made available on request.

Acknowledgements

The authors gratefully acknowledge financial support from the Spanish Ministerio de Ciencia e Innovación through project MCI-21-PID2020-113951GB-I00/AEI/10.13039/501100011033. Cristina Méndez-López also gratefully acknowledges the financial support through a “Severo Ochoa” grant (BP20-059) from the Principality of Asturias, Spain.

Appendix A. Supplementary data

Supplementary data to this article can be found online at https://doi.org/10.1016/j.sab.2024.106949.

References

[1] G. Galbács, A critical review of recent progress in analytical laser-induced breakdown spectroscopy, Anal. Bioanal. Chem. 407 (2015) 7537–7562.
[2] A. Giakoumaki, I. Osticioli, D. Anglos, Spectroscopic analysis using a hybrid LIBS-Raman system, Appl. Phys. A Mater. Sci. Process. 83 (2006) 537–541.
[3] Q. Lin, G. Niu, Q. Wang, Q. Yu, Y. Duan, Combined laser-induced breakdown with Raman spectroscopy: historical technology development and recent applications, Appl. Spectrosc. Rev. 48 (6) (2013) 487–508.
[4] J. Moros, M.M. ElFaham, J.J. Laserna, Dual-spectroscopy platform for the surveillance of Mars mineralogy using a decisions fusion architecture on simultaneous LIBS-Raman data, Anal. Chem. 90 (2018) 2079–2087.
[5] C. Latkkoczy, T. Ghislain, Simultaneous LIBS and LA-ICP-MS analysis of industrial samples, J. Anal. At. Spectrosc. 21 (2006) 1152–1160.
[6] M. Bonta, J. Gonzalez, C. Quarles Jr., R. Russo, B. Hegedus, A. Limbeck, Elemental mapping of biological samples by the combined use of LIBS and LA-ICP-MS, J. Anal. At. Spectrosc. 31 (2016) 252.
[7] L. Brunnbauer, M. Mayr, S. Larisegger, M. Nelhiebel, L. Pagnin, R. Wiesinger, M. Schreiner, A. Limbeck, Combined LA-ICP-MS/LIBS: powerful analytical tools for the investigation of polymer alteration after treatment under corrosive conditions, Sci. Rep. 10 (2020) 12513.
[8] X. Zeng, X. Mao, R. Greif, R. Russo, Experimental investigation of ablation efficiency and plasma expansion during femtosecond and nanosecond laser ablation of silicon, Appl. Phys. A Mater. Sci. Process. 80 (2005) 237–241.
[9] B. Verhoff, S. Harilal, J. Freeman, P. Diwakar, A. Hassanein, Dynamics of femto- and nanosecond laser ablation plumes investigated using optical emission spectroscopy, J. Appl. Phys. 112 (2012) 093303.
[10] T. Labutin, V. Lednev, A. Ilyn, A. Popov, Femtosecond laser-induced breakdown spectroscopy, J. Anal. At. Spectrom. 31 (1) (2016) 90–118.
[11] J. Singh, S. Thakur, Laser-Induced Breakdown Spectroscopy, Elsevier, Amsterdam, 2007.
[12] L. Cabalin, J. Laserna, Experimental determination of laser induced breakdown thresholds of metals under nanosecond Q-switched laser operation, Spectrochim. Acta Part B: At. Spectrosc. 53 (1998) 723–730.
[13] V. Babushok, F. DeLucia Jr., J. Gottfried, C. Munson, A. Miziolek, Double pulse laser ablation and plasma: laser induced breakdown spectroscopy signal enhancement, Spectrochim. Acta Part B. At. Spectrosc. 61 (2006) 999–1014.
[14] S. Harilal, J. Freeman, P. Diwakar, A. Hassanein, Femtosecond laser ablation: Fundamentals and applications, in: S. Musazzi, U. Perini (Eds.), Laser-Induced Breakdown Spectroscopy: Theory and Applications, Berlin Heidelberg, Berlin, Springer, 2014, pp. 143–166.
[15] E. Gamaly, A. Rode, Physics of ultra-short laser interaction with matter: from phonon excitation to ultimate transformations, Progr. Quant. Electron. 37 (2013) 215–323.
[16] O. Albert, S. Roger, Y. Glinec, J. Loulergue, J. Etchepare, C. Boulmer-Leborgne, J. Perrière, E. Millon, Time-resolved spectroscopy measurements of a titanium plasma induced by nanosecond and femtosecond lasers, Appl. Phys. A Mater. Sci. Process. 76 (2003) 319–323.
[17] D. Grojo, J. Hermann, A. Perrone, Plasma analyses during femtosecond laser ablation of Ti, Zr, and Hf, J. Appl. Phys. 97 (2005) 063306.
[18] S. Noël, J. Hermann, T. Itina, Investigation of nanoparticle generation during femtosecond laser ablation of metals, Appl. Surf. Sci. 253 (2007) 6310–6315.
[19] E. Axente, S. Noël, J. Hermann, M. Sentis, I. Mihailescu, Correlation between plasma expansion and damage threshold by femtosecond laser ablation of fused silica, J. Phys. D. Appl. Phys. 41 (2008) 105216.
[20] E. Kautz, E. Rönnebro, A. Devaraj, D. Senor, S. Harilal, Detection of hydrogen isotopes in Zircaloy-4 via femtosecond LIBS, J. Anal. At. Spectrom. 36 (2021) 1217.
[21] E. Kautz, D. Senor, S. Harilal, The interplay between laser focusing conditions, expansion dynamics, ablation mechanisms, and emission intensity in ultrafast laser-produced plasmas, J. Appl. Phys. 130 (2021) 204901.
[22] S. Harilal, N. Farid, J. Freeman, P. Diwakar, N. LaHaye, H. A, Background gas collisional effects on expanding fs and ns laser ablation plumes, Appl. Phys. A Mater. Sci. Process. 117 (2014) 319–326.
[23] S. Harilal, P. Diwakar, M. Polek, M. Phillips, Morphological changes in ultrafast laser ablation plumes with varying spot size, Opt. Express 23 (12) (2015) 15608.
[24] K. Anoop, S. Harilal, R. Philip, R. Bruzzese, S. Amoruso, Laser fluence dependence on emission dynamics of ultrafast laser induced copper plasma, J. Appl. Phys. 120 (2016) 185901.
[25] S. Zhang, Y. Shin, Hydrodynamic expansion and plume splitting of the ultrafast laser-induced plasma during ablation of multi-element metallic materials under atmospheric condition, J. Appl. Phys. 135 (8) (2024) 083101.
[26] H. Hou, B. Yang, X. Mao, V. Zorba, P. Ran, R. Russo, Characteristics of plasma plume in ultrafast laser ablation with a weakly ionized air channel, Opt. Express 26 (10) (2018) 13425.
[27] W. Xu, A. Chen, Q. Wang, D. Zhang, Y. Wang, S. Li, Y. Jiang, M. Jin, Generation of high-temperature and low-density plasma with strong spectral intensity by changing the distance between the focusing lens and target surface in femtosecond laser-induced breakdown spectroscopy, J. Anal. At. Spectrom. 34 (2019) 1018.
[28] A. Kramida, Y. Ralchenko, J. Reader, A. N. A. Team, NIST Atomic Spectra Database, National Institute of Standards and Technology, 2023 (Online).
[29] R. Hai, X. Mao, G. Chan, R. Russo, H. Ding, V. Zorba, Internal mixing dynamics of cu/Sn-Pb plasmas produced by femtosecond laser ablation, Spectrochim. Acta Part B 148 (2018) 92–98.
[30] V. Zorba, X. Mao, R. Russo, Femtosecond laser induced breakdown spectroscopy of cu at the micron/sub-micron scale, Spectrochim. Acta Part B: At. Spectrosc. 113 (2015) 37–42.
[31] C. Aragón, J. Aguilera, Characterization of laser induced plasmas by optical emission spectroscopy: a review of experiments and methods, Spectrochim. Acta Part B 63 (2008) 893–916.
[32] R. Pearse, A. Gaydon, The Identification of Molecular Spectra, Chapman and Hall, London, 1976.

[33] J. Luque, D. Crosley, LIFBASE: database and spectral simulation program, in: SRI International Report MP 98-021, 1998.
[34] H. Griem, Plasma Spectroscopy, McGraw-Hill, New York, 1964.
[35] N. Konjević, W. Wiese, Experimental stark widths and shifts for spectral lines of neutral and ionized atoms, J. Phys. Chem. Ref. Data Monogr. 19 (1990) 1307.
[36] M. Gigosos, V. Cardeñoso, New plasma diagnosis tables of hydrogen stark broadening including ion dynamics, J. Phys. B Atomic Mol. Phys. 29 (20) (1996) 4795–4838.
[37] D. Scuderi, O. Albert, D. Moreau, P. Pronko, J. Etchepare, Interaction of a laser-produced plume with a second time delayed femtosecond pulse, Appl. Phys. Lett. 86 (2005) 071502.
[38] S. Harilal, C. Bindhu, M. Tillack, F. Najmabadi, A. Gaeris, Plume splitting and sharpening in laser-produced aluminium plasma, J. Phys. D. Appl. Phys. 35 (2002) 2935–2938.
[39] M. Tanski, R. Barbucha, J. Mizeraczyk, S. Tofil, Imaging and emission spectroscopy of the submicrosecond plasma generated from copper substrate with nanosecond laser pulses, Appl. Opt. 59 (27) (2020) 8388.
[40] J. Hermann, S. Noël, T. Itina, E. Axente, M. Povarnitsyn, Correlation between ablation efficiency and nanoparticle generation during the short-pulse laser ablation of metals, Laser Phys. 18 (4) (2008) 374–379.
[41] N. Kuznetsov, Y. Raizer, Recombination of electrons in a plasma expanding into a vacuum, J. Appl. Mech. Tech. Phys. 6 (4) (1965) 6–12.
[42] P. Rumsby, J. Paul, Temperature and density of an expanding laser produced plasma, Plasma Phys. 16 (3) (1974) 247–260.
[43] V. Piñon, D. Anglos, Optical emission studies of plasma induced by single and double femtosecond laser pulses, Spectrochim. Acta Part B: At. Spectrosc. 64 (2009) 950–960.
[44] A. Santagata, A. De Bonis, P. Villani, R. Teghil, G. Parisi, Fs/ns-dual-pulse orthogonal geometry plasma plume reheating for copper-based alloys analysis, Appl. Surf. Sci. 252 (2006) 4685–4690.
[45] A. De Giacomo, M. Dell'Aglio, O. De Pascale, R. Gaudiuso, R. Teghil, A. Santagata, G. Parisi, Ns- and fs-LIBS of copper-based-alloys: a different approach, Appl. Surf. Sci. 253 (19) (2007) 7677–7681.
[46] L. Fornarini, R. Fantoni, F. Colao, A. Santagata, R. Teghil, A. Elhassan, M. Harith, Theoretical modeling of laser ablation of quaternary bronze alloys: case studies comparing femtosecond and nanosecond LIBS experimental data, J. Phys. Chem. A 113 (52) (2009) 14364–14374.
[47] G. Cristoforetti, A. De Giacomo, M. Dell'Aglio, S. Legnaioli, E. Tognoni, V. Palleschi, N. Omenetto, Local thermodynamic equilibrium in laser-induced breakdown spectroscopy: beyond the McWhirter criterion, Spectrochim. Acta Part B: At. Spectrosc. 65 (2010) 86–95.
[48] J. Serrano, J. Moros, J. Laserna, Molecular signatures in femtosecond laser-induced organic plasmas: comparison with nanosecond laser ablation, Phys. Chem. Chem. Phys. 18 (2016) 2398.